Review of sol–gel thin film formation

C.J. Brinker, A.J. Hurd, P.R. Schunk, G.C. Frye and C.S. Ashley

Sandia National Laboratories, Albuquerque, NM 87185-5800, USA

Sol–gel thin films are formed by gravitational or centrifugal draining accompanied by vigorous drying. Drying largely establishes the shape of the fluid profile, the timescale of the deposition process, and the magnitude of the forces exerted on the solid phase. The combination of coating theory and experiment should define coating protocols to tailor the deposition process to specific applications.

1. Introduction

Despite significant advances in technologies based on sol–gel thin film processing (e.g refs. [1–29]) there has been relatively little effort directed toward understanding the fundamentals of sol–gel coating processes themselves (see for example refs. [30–39]). This paper reviews recent studies that address the underlying physics and chemistry of sol–gel thin film formation by dip- (or spin-) coating. We first discuss the salient features of dip- and spin-coating with consideration of single component fluids and binary fluid mixtures. We then address the deposition of inorganic sols with regard to timescales, drying theory, tendency toward cracking, and development of microstructure. We conclude with a discussion of topics for future study.

2. Dip-coating

In dip-coating, the substrate is normally withdrawn vertically from the coating bath at a constant speed, U_0 (see fig. 1) [40]. The moving substrate entrains the liquid in a fluid mechanical boundary layer that splits in two above the liquid bath surface, returning the outer layer to the bath [38]. Since the solvent is evaporating and drain-

ing, the fluid film acquires an approximate wedge-like shape that terminates in a well-defined drying line ($x = 0$ in fig. 1). When the receding drying line velocity equals the withdrawal speed, U_0, the process is steady state with respect to the liquid bath surface [39]. For alcohol-rich fluids common to sol–gel dip-coating, steady state conditions are attained in several seconds.

The hydrodynamic factors in dip-coating (pure liquids, ignoring evaporation) were first calculated correctly by Landau and Levich [41] and recently generalized by Wilson [42]. In an excellent review of this topic, Scriven [38] states that the thickness of the deposited film is related to the position of the streamline dividing the upward and downward moving layers. A competition between as many as six forces in the film deposition region governs the film thickness and position of the streamline: (1) viscous drag upward on the liquid by the moving substrate; (2) force of gravity; (3) resultant force of surface tension in the concavely shaped meniscus; (4) inertial force of the boundary layer liquid arriving at the deposition region; (5) surface tension gradient; and (6) the disjoining (or conjoining) pressure (important for films less than 1 μm thick).

When the liquid viscosity, η, and substrate speed are high enough to lower the curvature of
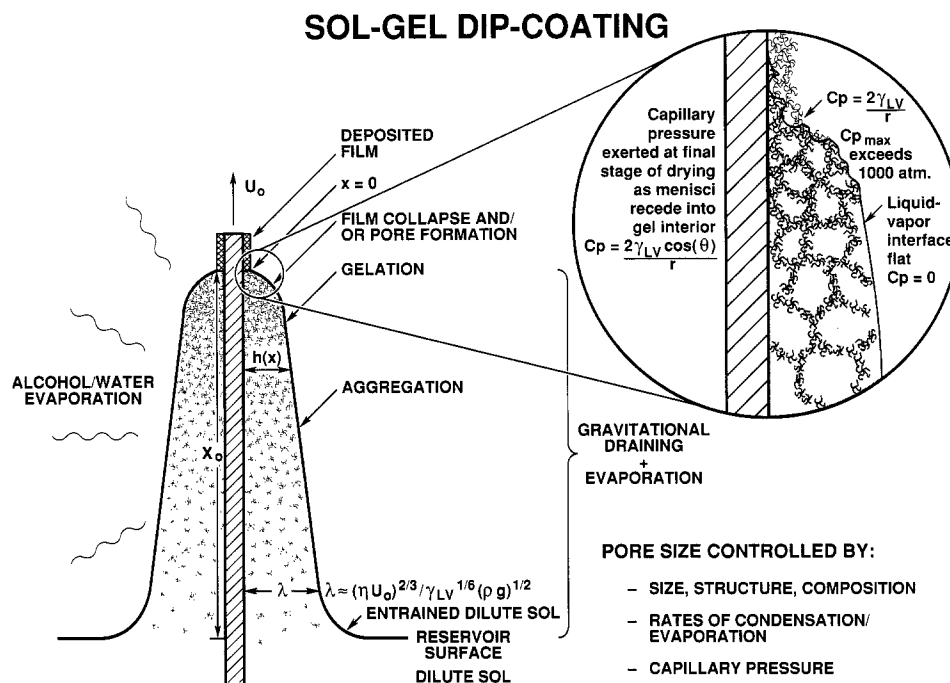
SOL-GEL DIP-COATING

Fig. 1. Schematic of the steady state dip-coating process, showing the sequential stages of structural development that result from draining accompanied by solvent evaporation, continued condensation reactions, and capillary collapse.

the gravitational meniscus, the deposited film thickness, h, is that which balances the viscous drag ($\propto \eta U_0/h$) and gravity force ($\rho g h$) [38]:

$$h = c_1(\eta U_0/\rho g)^{1/2}, \tag{1}$$

where the constant c_1 is about 0.8 for Newtonian liquids. When the substrate speed and viscosity are low (often the case for sol–gel film deposition), this balance is modulated by the ratio of viscous drag to liquid–vapor surface tension, γ_{LV}, according to the relationship derived by Landau and Levich [41]:

$$h = 0.94(\eta U_0)^{2/3}/\gamma_{LV}^{1/6}(\rho g)^{1/2}. \tag{2}$$

Figure 2 plots the logarithm of the product of thickness and refractive index minus 1 * versus the logarithm of U_0 for films prepared from a variety of silicate sols in which the precursor

* Since the quantity $(n-1)$ is proportional to the volume fraction solids, ϕ, the product $h(n-1)$ is proportional to the mass per unit area of film and takes into account the film porosity.

structures ranged from rather weakly branched polymers characterized by a mass fractal dimension to highly condensed particles [40]. The slopes are quite close to 0.66 in keeping with the expectations from eq. (2). This reasonable correspondence between the thickness of the deposited
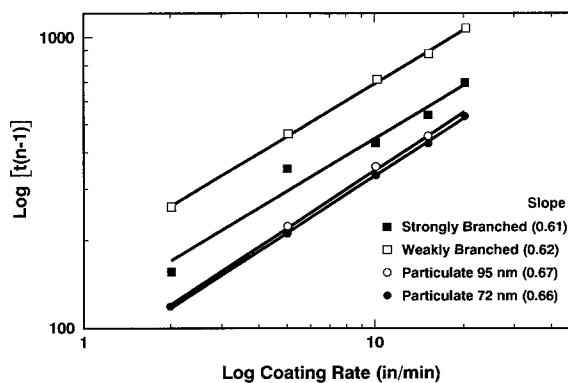

Fig. 2. Product of film thickness and refractive index minus 1 (proportional to film mass/unit area) versus withdrawal rate plotted according to eqs. (1) or (2).

films and a theory developed for gravitational draining of *pure fluids* suggests that the entrainment of the inorganic species has little effect on the hydrodynamics of dip-coating, at least in the early stages of deposition where the entrained sol is quite dilute. Thus, some insight into sol–gel film deposition may be gained by closer examination of the details of gravitational draining (and evaporation) of pure (and binary) fluids.

2.1. Film thickness profiles during dip-coating: pure fluid

Previous theories of gravitational draining of pure fluids have not taken into account simultaneous evaporation. Although the thickness of the fluid entrained at the bath surface is apparently not sensitive to evaporation, the film is progressively thinned by evaporation as it is transported by the substrate away from the coating bath. For depositing sols, thinning by evaporation causes a corresponding increase in sol concentration, hence an understanding of simultaneous draining and evaporation is essential to the underlying physics of sol–gel film deposition.

In order to address this problem, Hurd and Brinker [39] developed an imaging ellipsometer

that allows aquisition of spatially resolved thickness and refractive index data over the entire area of the depositing film. A thickness profile of an ethanol film obtained by imaging ellipsometry is shown in fig. 3 [43]. Instead of the wedge expected for a constant evaporation rate, the film profile is distinctly blunt near the drying line ($x = 0$ in figs. 1 and 3), indicative of more rapid thinning and, hence, a greater evaporation rate there.

This position sensitive evaporation rate is a consequence of the film geometry: the blade-like shape of the depositing film in the vicinity of the drying line enhances the rate of diffusion of vapor away from the film surface [43] (at large x, the strongest concentration gradients of vapor are normal to the surface, while near $x = 0$, stronger gradients are established parallel to the surface). Near any sharp boundaries, the evaporation rate, E, diverges, but the vaporized mass must remain integrable. For the knife blade geometry (infinite sheet), E varies with x as follows [43]:

$$E(x) = -D_v a_1 x^{-1/2}, \tag{3}$$

where D_v is the diffusion coefficient of the vapor (~ 0.1 cm^2/s) and a_1 is a constant. Since thickness varies inversely with evaporation rate, the
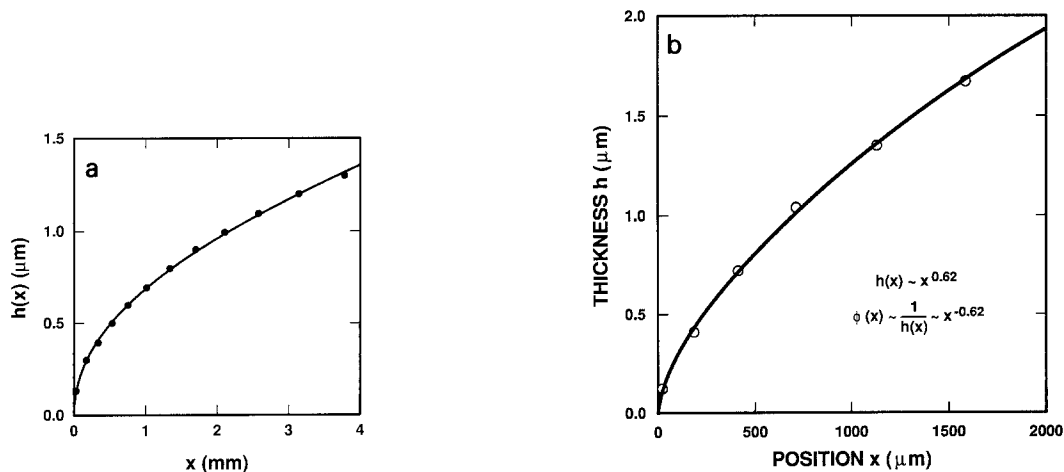

Fig. 3. (a) Thickness profile of dip-coated ethanol film (solid dots). The profile is quite well fit by the form $h \sim x^\nu$ with $\nu = 0.5 \pm 0.01$ (solid line). From Hurd and Brinker [43]. (b) Thickness profile of a titanate sol during dip-coating as determined by imaging ellipsometry. Position x is defined in fig. 1. From Brinker et al. [37].

divergence in the evaporation rate as $x \to 0$ accounts for the blunt profile shown in fig. 3, where the data are fit to the form

$$h(x) \sim 1/E(x) \sim x^\nu, \quad \nu = 0.50 \pm 0.01, \tag{4}$$

according to the expectations from eq. (3).

The singularity strength (exponent) in eq. (4) is sensitive to the geometry of the film. For coating a fiber, we would expect a logarithmic singularity [44], and as a coated cylinder decreases in radius, the profile should pass smoothly from $x^{1/2}$ toward $\ln x$. Although some .experimental evidence exists for this behavior by extrapolating to small cylinder diameters [44], it is a difficult proposition to prove experimentally. Surface tension effects make it difficult to coat a fiber fast enough for the drying line to be well-separated from the gravitational meniscus at the reservoir surface.

2.2. Film thickness profiles during dip-coating: binary fluid

The most common coating sols are composed of two or more miscible liquids, e.g., ethanol–water. Differences in their evaporation rates and surface tensions alter the shape of the fluid profile in the vicinity of the drying line and, in some cases, create rib-like instabilities in a region near the liquid bath surface. Ellipsometric images [44] of depositing alcohol–water films show two roughly parabolic features (fig. 4), that correspond to successive drying of the alcohol- and water-rich regions, according to the non-constant evaporation model (eq. (4)). This suggests that each component has an independent evaporation singularity. If the water-rich phase is denoted as phase 1 and ethanol is phase 2, then the independent profiles are additive:

$$h_1 = a_1 x^{1/2}, \qquad x > 0, \tag{5}$$

$$h_2 = a_2(x - x_2)^{1/2}, \quad x > x_2, \tag{6}$$

$$h_2 = 0, \qquad x < x_2, \tag{7}$$

where h is the total thickness, $h_1 + h_2$, and x_2 is the position of the 'false' drying line created by the substantial depletion of ethanol.
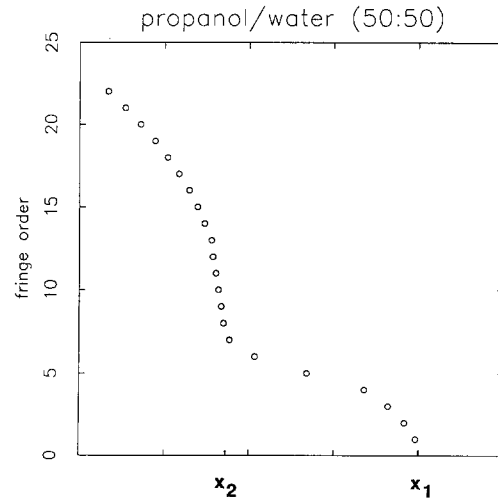

Fig. 4. Thickness profile of 50:50 propanol:water film (volume ratio). The double parabolic profile is due to differential volatilities and surface tension gradient driven flows. x_1 is the position of the drying line; x_2 is the position of the 'false' drying line created by the depletion of the ethanol-rich phase. Film thickness equals approximately the fringe order times 240 nm. From Hurd [44].

The 'foot' feature in fig. 4 typical of binary solvents is not due to differential volatility alone. Since each component has a different surface tension, γ, surface tension gradients are established [44]:

$$d\gamma/dx = (\gamma_1 - \gamma_2)\, d\phi_1/dx \quad (x > x_2)$$

$$= 0 \ (0 < x < x_2), \tag{8}$$

where the surface tension is assumed to follow a simple mixing law, $\gamma = \phi_1\gamma_1 + \phi_2\gamma_2$ where ϕ_i is the volume fraction of component i. ** Since at the liquid–vapor boundary the viscous shear force must balance the force imposed by surface tension gradients, $\eta \ du/dz = d\gamma/dx(z = h)$, liquid flows into the water-rich foot with velocity, u:

$$u = 1/\eta[d\gamma/dx]z - u_0, \tag{9}$$

the so-called 'Marangoni effect'. The foot slowly

** For ethanol–water mixtures, the surface tension does not obey a simple linear mixing law. The surface tension can be approximated by $1/(\gamma^{2.7}) \approx \phi_H /(\gamma_H^{2.7}) + \phi_E /(\gamma_E^{2.7})$ where the subscripts H and E refer to water and ethanol, respectively [69].

grows until this flux is balanced by that of evaporation from the expanding free surface.

The surface tension gradient driven flow of liquid through the thin neck created by the preferential evaporation of alcohol can create quite high shear rates during dip-coating. A striking example is that of toluene and methanol [44]. The surface tension gradient driven flows are strong enough to greatly distort the double parabolic profile. The film thins then thickens, creating a 'pile-up' of toluene near the drying line. A crude estimate of the surface tension gradient, $\Delta\gamma/\Delta x \simeq (10 \text{ dyn/cm})/10^{-1}$ cm, leads to a shear rate, $\mathrm{d}u/\mathrm{d}z \simeq 10^4 \text{ s}^{-1}$, in the thin region, from eq. (9), assuming $\eta = 0.01$ P. Conceivably these shear fields may be sufficiently strong to align or order the entrained inorganic species.

3. Spin-coating

Spin-coating differs from dip-coating in that the depositing film thins by centrifugal draining and evaporation. Bornside et al. [45] divide spin-coating into four stages: deposition, spin-up, spin-off and evaporation, although for sol–gel coating, evaporation normally overlaps the other stages. An excess of liquid is dispensed on the surface during the deposition stage. In the spin-up stage, the liquid flows radially outward, driven by centrifugal force. In the spin-off stage, excess liquid flows to the perimeter and leaves as droplets. As the film thins, the rate of removal of excess liquid by spin-off slows down, because the thinner the film, the greater resistance to flow, and because the concentration of the non-volatile components increases, raising the viscosity. In the final stage, evaporation takes over as the primary mechanism of thinning.

According to Scriven [38], an advantage of spin-coating is that a film of liquid tends to become uniform in thickness during spin-off and, once uniform, tends to remain so, provided that the viscosity is not shear-dependent and does not vary over the substrate. This tendency is due to the balance between the two main forces: centrifugal force, which drives flow radially outward, and viscous force (friction), which acts radially

inward. The thickness of an initially uniform film during spin-off is described by

$$h(t) = h_0/\left(1 + 4\rho\omega^2 h_0^2 t/3\eta\right)^{1/2} \qquad (10)$$

where h_0 is the initial thickness, t is time, ρ is the density, and ω is the angular velocity. Even films that are not initially uniform tend monotonically toward uniformity, sooner or later following eq. (10).

Equation (10) pertains to Newtonian liquids that do not exhibit a shear rate dependence of the viscosity during the spin-off stage. If the liquid is shear-thinning (often the case for aggregating sols), the lower shear rate experienced near the center of the substrate causes the viscosity to be higher there and the film to be thicker. This problem might be avoided by metering the liquid from a radially moving arm during the deposition/spin-up stage.

4. Effects of entrained condensed phases

The preceding discussion has ignored the effects of the entrained inorganic species, either polymers or particles, on the film deposition process. During dip-coating, these species are initially concentrated by evaporation of solvent as they are transported from the coating bath toward the drying line within the thinning fluid film (see fig. 1). Steady-state conditions in this region require conservation of non-volatile mass; thus, the solids mass in any horizontal slice of the thinning film must be constant [43]:

$$h(x)\phi_s(x) = \text{constant}, \qquad (11)$$

where ϕ_s is the volume fraction solids. From eq. (11), we see that ϕ_s varies inversely with h. Since for a planar substrate we expect a parabolic thickness profile, ϕ_s should vary as $1/h \simeq x^{-1/2}$ in the thinning film. When coating a fiber, we expect $\phi(x) \sim (\ln x)^{-1}$.

The rapid concentration of the entrained inorganic species by evaporation is more evident from consideration of the mean particle (polymer) separation distance, $\langle r \rangle$, which varies as the inverse cube root of ϕ, $\langle r \rangle \sim x^{1/6}$. This is a very precipitous function: half the distance between particle

C.J. Brinker et al. / Sol–gel thin film formation   429

(polymer) neighbors is traveled in the last 2% of the deposition process ($\sim$ 0.1 s). The centrifugal acceleration needed to cause an equivalent rate of crowding is as much as 10^6 G's! [§] The increasing concentration can lead to aggregation, network formation, or a colloidal crystalline state, altering the sol rheology from Newtonian (dilute conditions) to shear-thinning (aggregated systems) or thixotropic (ordered systems). For polymeric sols, the reduced viscosity shows a strong concentration dependence [46], and, in general, the viscosity increases abruptly at high concentrations. Bornside et al. [45], in their studies of spin-coating, assumed the following relationship:

$$\eta = \eta_0(1 - \chi_A)^4 + \eta_s, \qquad (12)$$

where η is the viscosity of the sol, η_s is the viscosity of the solvent, η_0 is the viscosity of the polymer, and χ_A is the mass fraction of solvent.

In dip-coating, the thickness of the entrained film ($\propto U_0^{2/3}$) and the evaporation rate establish the timescale of the deposition process, which is typically several seconds. The forced convection created during spin-coating increases the evaporation rate, establishing an even shorter timescale. These short timescales significantly reduce the time available for aggregation, gelation, and aging compared with bulk gel formation. We anticipate several consequences of the short timescale of the film deposition processes.

(1) There is little time available for reacting species to 'find' low energy configurations. Thus (for reactive systems) the dominant aggregative process responsible for network formation may change from reaction-limited (near the reservoir surface) to transport-limited near the drying line.

(2) For sols composed of repulsive particles, there is little time available for the particles to order as they are concentrated in the thinning film.

(3) There is little time available for condensation reactions to occur. Thus gelation may actually occur by a physical process, through the

[§] This assumes that there exists no steric barriers to concentration; often aggregation/network formation will interupt this dramatic compaction process.

concentration dependence of the viscosity (e.g., eq. (12)), rather than a chemical process. (In some systems this is evident by the fact that the deposited film is quickly re-solubilized when immersed in solvent.)

(4) Since the gels are most likely more weakly condensed and hence more compliant than bulk gels, they are more easily compacted, first by evaporation and then by the capillary pressure exerted at the final stage of the deposition process (see fig. 1). In such compliant materials the effects of capillary forces are enhanced, because greater shrinkage precedes the critical point, causing the pore size to be smaller and the maximum capillary pressure to be greater.

5. Drying of films

5.1. Capillary pressure

As stated above, drying accompanies both the dip- and spin-coating processes and largely establishes the shape of the fluid film profile. The increasing concentration that results from drying often leads to the formation of an elastic or viscoelastic gel-like state. Further evaporation gives rise to capillary tension in the liquid, P, and that tension is balanced by compressive stresses on the solid phase, causing it to contract further [47]. The maximum capillary tension occurs at the critical point, when the menisci enter the pores, and the radius of curvature of the meniscus, r_m, is related to the pore radius, r_p, by $r_m = r_p/\cos\theta$, where θ is the contact angle of the receding meniscus within the emptying pore [47]. Then the tension at the drying surface is given by Laplace's equation:

$$P_{max} = 2\gamma_{LV}/r_m = 2\gamma_{LV}\cos(\theta)/r_p. \qquad (13)$$

Since r_p can be of molecular dimensions, the magnitude of P_{max} can be very large. Using values of minimum menisci radii, r_{min}, determined from desorption isotherms and assuming complete wetting ($\cos\theta = 1$), it is possible to estimate from eq. (13) the maximum capillary tension of the liquid prior to tensile failure [48]. For ethanol ($\gamma_{LV} = 22.75$ dyn/cm at 20°C), r_{min} is estimated to be

about 1.3 nm, and $P_{max} \simeq 348$ bar. For water ($\gamma_{LV}/ = 72.8$ dyn/cm at 20°C), r_{min} is estimated to range from 1.1 to 1.55 nm, so P_{max} ranges from 940 to 1320 bar! These large tensile pressures drive the solvent into metastable states analogous to superheating. Burgess and Everett suggest that the liquid does not boil, because nucleation cannot occur in such small pores [49].

Very little shrinkage occurs after the menisci recede into the pores, so the pore size in a dry gel is largely established by the forces exerted at the critical point [47]. For very compliant materials, the network cannot resist the capillary forces (which increase continuously as r_p decreases toward r_{min}), so there is no critical point, and the pores collapse completely [37,50]. Conversely, for stiffer materials, shrinkage ceases at an earlier stage of drying, causing r_p to be larger and P_{max} to be smaller. This situation leads to porous films.

5.2. Stages of drying

Scherer [40,47] divides the drying of gels into two stages: a constant rate period (CRP) and a falling rate period. During the constant rate period, mass transfer is limited by convection away from the gel surface, whereas during the falling rate period, mass transfer is limited by the permeability of the gel. Extending these ideas to dip-coating, we might expect that a CRP would obtain throughout most of the deposition process, since the liquid–vapor interface remains located at the exterior surface of the thinning film except at the final stage of drying (see fig. 1). A constant evaporation rate implies a wedge-shaped film profile. This is not observed for pure fluids, nor is it observed for inorganic sols. Figure 3(b) shows the film profile of a titanate sol prepared in ethanol. Thickness varies with distance from the drying line as $h(x) \sim x^{0.62}$, which indicates that the evaporation rate increases as $x \to 0$ (see eqs. (3) and (4)) although not as rapidly as for pure ethanol ($h(x) \sim x^{0.5}$). Thus, even for the deposition of inorganic sols, the film profile, and hence the concentration profile, are largely established by the dependence of the evaporation rate on the geometry of the depositing film. For sols containing fluid mixtures of differing volatilities, the fluid

composition changes with distance, x, contributing to further changes in the evaporation rate. In the CRP, the rate of drying is usually calculated from an external mass transfer correlation such as [51]

$$\text{mass flux/unit area} = k_{mt}(\rho_s - \rho_\infty), \quad (14)$$

where ρ_s is the theoretical density of solvent in equilibrium with the surface of the coating, ρ_∞ is the theoretical density of solvent vapor far removed from the coating surface, and k_{mt} is the mass transfer coefficient (m/s). For modeling sol–gel dip-coating, k_{mt} must be position-dependent.

The critical point should mark the beginning of the falling rate period. Depending on the distribution of the liquid in the pores, for example funicular or pendular, the drying rate is limited by flow (funicular state) or diffusion (pendular state) [40]. For compliant molecular networks that are collapsed prior to the critical point, drying occurs by Fickian diffusion if the temperature is above the glass transition temperature of the mixture [52]. The onset of a falling rate period near the drying line may account for the differences in the exponents that describe the shape of the pure fluid and the titanate sol film profiles (compare figs. 3(a) and 3(b)).

5.3. Drying stress and cracking

As the film dries, it shrinks in volume. Once the film is attached to the substrate and unable to shrink in that direction, the reduction in volume is accommodated completely by a reduction in thickness. When the film has solidified and stresses can no longer be relieved by flow, tensile stresses develop in the plane of the substrate. Croll [53] estimated the stress, σ, as

$$\sigma = [E/(1-\nu)][(f_s - f_r)/3] \quad (15)$$

where E is Young's modulus (Pa), ν is Poisson's ratio, f_s is the volume fraction solvent at the solidification point, and f_r is the volume fraction of residual solvent in the 'dry' film. The solidification point was defined for a polymer film as the concentration where the glass transition temperature has risen to the experimental temperature.

Thus stress is proportional to Young's modulus and the difference between the fraction solvent at the solidification point and the dried coating. Scherer [40,47] states that the stress in the film is very nearly equal to the tension in the liquid ($\sigma \simeq P$). Despite such a large stress, it is commonly observed that cracking of films does not occur if the film thickness is below a certain critical thickness $h_c \simeq 0.5$–1 μm [40]. For films that adhere well to the substrate, the critical thickness for crack propagation or the growth of pinholes is given by [54,55]

$$h_c = (K_{Ic}/\sigma\Omega)^2 \tag{16}$$

where K_{Ic} is the critical stress intensity and Ω is a function that depends on the ratio of the elastic modulus of the film and substrate (for gel films $\Omega \simeq 1$). For films thinner than h_c, the energy required to extend the crack is greater than the energy gained from relief of stresses near the crack, so cracking is not observed [40].

When the film thickness exceeds h_c, cracking occurs, and the crack patterns observed experimentally are qualitatively consistent with fractal patterns predicted by computer simulation [56]. Atkinson and Guppy [57] observed that the crack spacing increased with film thickness and attributed this behavior to a mechanism in which partial delamination accompanies crack propagation. Such delamination was observed directly by Garino [58] during the cracking of sol–gel silicate films.

Based on eqs. (15) and (16) above, strategies to avoid cracking include: (1) increasing the fracture toughness, K_{Ic}, of the film, (2) reducing the modulus of the film, (3) reducing the volume fraction of solvent at the solidification point, and (4) reducing the film thickness. In organic polymer films, plasticizers are often added to reduce the stiffness of the film and thus avoid cracking [51]. For sol–gel systems, analogous results are obtained by organic modification of alkoxide precursors [32], chelation by multidentate ligands such as β-diketonates [59], or a reduction in the extent of hydrolysis of alkoxide precursors [158].

It should be noted that for particulate films Garino [60] observed that the maximum film thickness obtainable without cracks decreased linearly with a reduction in particle size. Since, for unaggregated particulate films, the pore size scales with the particle size, this may be due to an increase in the stress caused by the capillary pressure ($\sigma \simeq P$) and/or an increase in the volume fraction solvent at the solidification point resulting from the manner in which the electrostatic double layer thickness (estimated by the Debye–Huckel screening length) varies with particle size [40].

6. Control of microstructure

The final film microstructure depends on the structure of the entrained inorganic species in the original sol (for example, size and fractal dimension), the reactivity of these species (for example, condensation or aggregation rates), the timescale of the deposition process (related to evaporation rate and film thickness), and the magnitude of shear forces and capillary forces that accompany film deposition (related to surface tension of the solvent or carrier and surface tension gradients). The most common means of controlling the film microstructure is to control the particle size. For unaggregated monosized particulate sols, the pore size decreases and the surface area increases with decreasing particle size. Asymmetric, supported membranes have been prepared successfully from particulate sols for use in ultrafiltration [18,19]. As noted above, difficulties arise when trying to prepare microporous membranes due to an increased tendency for cracking. Particulate sols may be intentionally aggregated prior to film formation to create very porous films (e.g., > 65 vol.% porosity) [40]. For electrostatically stabilized silica sols, a transition from random close packing to ordered packing is observed with increasing substrate withdrawal rates, U_0. This may be due to a longer timescale of the deposition process (providing more time for ordering) or an increase in the shear rate accompanying deposition for higher U_0 [37].

A second strategy for controlling porosity is based on the scaling of mass, M_f, and size, r_f, of a mass fractal object [40]:

$$M_f \sim r_f^D, \tag{17}$$

Table 1

Refractive index, % porosity, pore size, and surface area of multicomponent silicate films versus sol aging times prior to film deposition

Sample aging times [a]	Refractive index	Porosity [b] (%)	Median pore radius (nm)	Surface area (m^2/g)	Applications
unaged	1.45		< 0.2	1.2–1.9	Dense protective, electronic and optical films
0–3 days					Microporous films for sensors and membranes
3 days	1.31	16	1.5	146	Mesoporous films for sensors, membranes, catalysts, optics
1 week	1.25	24	1.6	220	
2 week	1.21	33	1.9	263	
3 week [c]	1.18	52	3.0	245	

[a] Aging of dilute sol at 50°C and pH3 prior to film deposition.

[b] Determined from N$_2$ adsorption isotherm.

[c] The 3-week sample gelled. It was re-liquified at high shear rates and diluted with ethanol prior to film deposition.

where D is the mass fractal dimension (in three-dimensional space, $0 < D < 3$). Since density equals mass/volume, the density, ρ_f, of a mass fractal object varies in three dimensional space as $\rho_f \sim r_f^D/r_f^3$, and the porosity varies as $1/\rho_f \sim r_f^{(3-D)}$. Thus, the porosity of a mass fractal object increases with its size. Providing that such fractals do not completely interpenetrate during film formation (i.e., they are mutually opaque, requiring $D > 1.5$ [40]), the porosity may be controlled by the size of the entrained fractal species prior to film formation. The efficacy of this approach is illustrated in table 1 [37] where the refractive index, % porosity, pore size, and surface area are seen to vary monotonically with aging time employed to grow the fractal species prior to film deposition. [§§] The extent of interpenetration of colliding fractals depends on their respective mass fractal dimensions and the condensation rate or 'sticking probability' at points of intersection. A reduction of either D or the condensation rate increases the interpentration and decreases the porosity [37,40]. From eq. (17) and surrounding

[§§] The film porosity, pore size, and surface area were measured in situ using a surface acoustic wave technique developed by Frye et al. [14].

discussion, it follows that, to generate porosity using this fractal scheme, r_f should be large, $1.5 \ll D \ll 3$, and the condensation rate should be high. Conversely dense films should be formed from small, unreactive precursors consistent with observation [61].

The magnitude of the capillary pressure, P_{max}, should also be quite influential in determining microstructure. For bulk gels, elimination of surface tension by supercritical processing results in highly porous aerogels. Deshpande et al. have recently shown that, for aprotic pore fluids, the surface area, pore volume, and pore size of bulk silica xerogels are all reduced monotonically by an increase in surface tension of the pore fluid [62]. Such studies are more difficult for films, since it is not possible to wash the coating sol and distillation of solvents often leads to premature gelation. The most revealing studies are those comparing the effects of different hydrolysis ratios, $H_2O/M(OR)_n$, on film properties. Since the theoretical ratio for complete hydrolysis and condensation is $n/2$, greater ratios must produce 'excess' water. As described above, in mixed solvent systems, the least volatile component survives to the drying line and therefore dictates the magnitude of the capillary pressure, P_{max}. In

mixed alcohol/water systems, the composition of the fluid near the drying line is enriched in water due to preferential evaporation of alcohol and surface tension gradient driven flows. We have shown that as the vol.% 'excess' water is increased from 0.5 to 6.0 vol.%, the refractive index of silica films deposited by dipping increases from 1.342 to 1.431, corresponding to a reduction in porosity from 22 to 7% [63]. Further increases in the excess water content cause a reduction in refractive index (increase in porosity). Since water increases both the surface tension and the extent of condensation of the silicate matrix, this behavior reflects the competition between capillary pressure, which compacts the film, and aging, which stiffens the film increasing its resistance to compaction. These results differ from those of Glaser and Pantano [64] who observed a monotonic increase in refractive index with water concentration for spin-coated silicate films. The difference between dip- and spin-coating is the evaporation rate and correspondingly the time available for aging. Spinning creates a strong forced convection in the vapor above the substrate [38], increasing the evaporation rate. Thus there is little time for aging to occur, and the structure of the film is dominated by the effects of capillarity. In a similar dip-coating study, Warren et al. [12] observed that, for silica films annealed at 800°C, the dielectric strength increased and the HF etch rate decreased as the hydrolysis ratio of the coating sol increased from 1 to 7.5. Further increases caused the reverse behavior. This implies that the effects of capillarity and aging also strongly influence the subsequent consolidation process.

Finally, it is anticipated that shear forces accompanying film formation could influence microstructure. Although the withdrawal rates, U_0, are often very low in dip-coating, we have shown that surface tension gradient driven flows can cause high shear rates (10^4 s^{-1}) near the drying line. Such shear rates might be partially responsible for the ordering of monosized particulate films [63]. Spin-coating is characterized by higher shear rates. Several studies have shown that the refractive index increases or decreases with increasing rotational speed [40,64]. Presumably

these conflicting results are explainable by consideration of the effects of both time scale and shear on microstructural development: increasing the rotational speed increases the shear rate and reduces the characteristic time scale.

7. Topics for further study

7.1 Modeling

Accurate theories of dip- and spin-coating would permit better control of these processes and would allow the design of specific coating protocols for specific applications. Both dip- and spin-coating are transient processes of flow and mass transfer. Falling diffusivity, rising viscosity, and changing rheology as solvents evaporate from the remaining film further complicate the process. Bornside et al. [46] have outlined the basic principles of the flow mechanics, solvent transport, and film formation during spin-coating. Schunk [65] has developed a finite element model of the complete convective-diffusion problem associated with dip-coating an ethanol–water mixture. His strategy is to combine the theory of convection and diffusion in the liquid with a mass transfer model in the gas. Models and constitutive equations are used to account for liquid–vapor equilibria and surface tension. Thus far thermal effects induced by latent heat of evaporation and diffusion-driven convection are neglected [+] and water is assumed to be relatively non-volatile. Conservation of mass and momentum (of both liquid and volatile species) leads to solutions for the position of the free surface (which locates according to the capillary hydrodynamic forces and ethanol loss by evaporation) and the concentration profiles as shown in fig. 5 [65]. Preferential evaporation of ethanol enriches the free (liquid–vapor) surface in water. In the vicinity of the drying line, the more volatile alcohol may be substantially depleted, leaving behind a water-rich film. He finds that the concentration

---

[+] Bornside et al. [45] have shown that, for spin-coating with volatile solvents, the temperature change of the depositing fluid is negligible ($\ll$ 1 K at 3000 rpm).

contours in the thinning film are very sensitive to the composition of the overlying vapor phase. This suggests the possibility of managing the solvent partial pressure to gain more control of the process. A similar conclusion was arrived at by Bornside et al. for spin-coating [45].

7.2 In situ characterization of film deposition

Deficiencies in modeling efforts arise due to the lack of available data concerning changing viscosity, solvent composition, capillary pressure, mechanical properties, etc., during coating. The steady-state film profile established during dip-coating creates an opportunity to acquire optical or spectroscopic data as a function of height above the reservoir surface and thus to provide information about the continually changing environment within the depositing film. Imaging ellip-
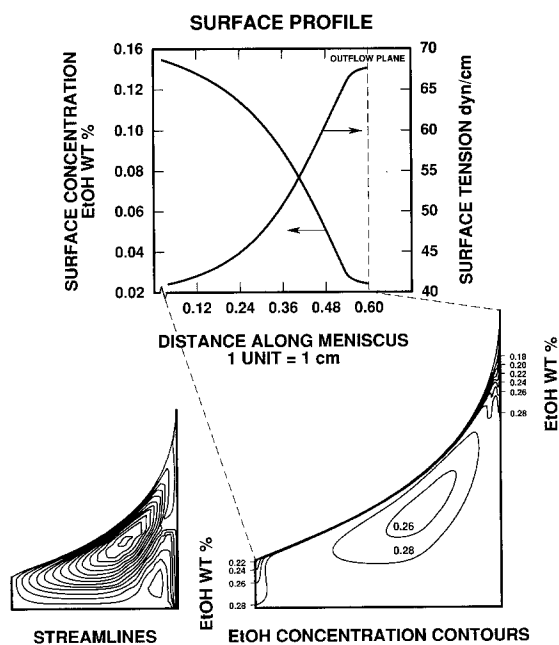

Fig. 6. Emission spectra of pyrene in silicate coating sol (1×10^{-3} M) and in corresponding film prepared by dip-coating.

sometry [39] has proven to be extremely valuable in determining thickness and refractive index profiles. FTIR microscopy [37] has been employed to monitor changes in solvent composition. A related approach is to use various fluorescent molecules, ions, or crystals as photophysical or photochemical probes. The probes are entrained in the depositing film and transported to the drying line along with the dispersed inorganic phase. Acquisition of emission spectra as a function of height above the reservoir surface should provide structural information related to the surroundings of the probe on a length scale of one to several nanometers. This approach has been used successfully to characterize gelation, aging, and drying in bulk systems [66,67]. It benefits from the availability of literally thousands of potential probes that are sensitive to changes in viscosity, solvent polarity, local geometry, rigidity, pressure, etc. Figure 6 compares the emission spectrum of pyrene in the coating sol and in the corresponding film. Changes in intensity of the PyPy* emission band at 470 nm are attributed to changes in the geometry, surface irregularity, and/or porosity of the film [66]. N_2 adsorption–desorption isotherms, obtained for the film using a SAW technique indicate that this film is completely collapsed during drying [37]: there are no pores accessible to N_2 (kinetic diameter $\simeq 0.4$ nm). Trapping of pyrene within such small 'pores' apparently precludes excimerization, $Py + Py^* \rightarrow PyPy^*$.

Fig. 5. Fluid streamlines and EtOH concentration contours of 30 wt% EtOH–70 wt% H_2O solution during dip-coating predicted by the finite element model. The overlying saturation of EtOH was assumed to vary linearly from 10% at the reservoir surface to 0% at the drying line. The change in ethanol concentration along the free (liquid–vapor) surface results in a steep gradient in surface tension. Substrate is represented in the bottom two plots by the vertical line on the right. From Schunk et al. [65].
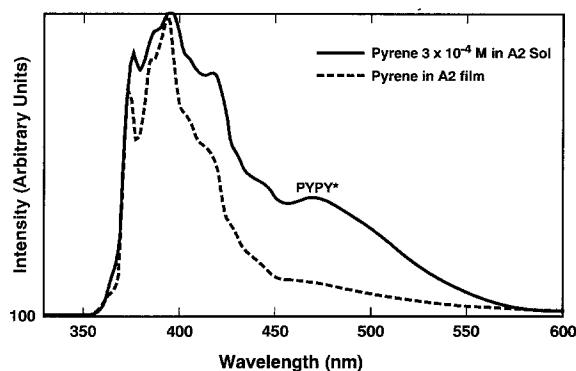
7.3 Development of porosity in non-silicate films

The control of porosity in silicate films is facilitated by the wide range of silicate sol structures that result from changes in synthesis parameters such as choice of catalyst and hydrolysis ratio. Due to the much faster hydrolysis and condensation rates of alkoxides of more electropositive elements such as Ti or Zr, it has proven difficult to synthesize polymers with an equivalent range of structural diversity. Multidentate molecules such as β-diketonates, glycols, or alcohol amines have been used successfully to chelate the metal alkoxides and thus retard reaction rates, but to date control of molecular weight, extent of branching, and fractal dimensionality has not been documented [68]. If stable fractal structures could be prepared, aggregation could be exploited (rather than avoided) to form films with a range of porosities as demonstrated for silicates (see table 1).

References

[1] W. Geffcken and E. Berger, Deutsches Reichspatent 736411, May 6, 1939 (Jenaer Glaswerk Schott&Gen., Jena)

[2] H. Dislich, in: Sol–Gel Technology for Thin Films, Fibers, Preforms, Electronics, and Specialty Shapes ed. L.C. Klein (Noyes, Park Ridge, NJ, 1988) p. 50.

[3] H. Schroeder, in: Physics of Thin Films, Vol. 5, ed. H. Haas (Academic Press, New York, 1969) p. 87.

[4] R.L. Nelson, J.D.F. Ramsay, J.L. Woodhead, J.A. Cairns and J.A.A. Crossley, Thin Solid Films 81 (1981) 329.

[5] D.P. Partlow and T.W. O'Keeffe, Appl. Opt. 29 (1990) 1526.

[6] H.G. Floch, J.-J. Priotton and I.M. Thomas, Thin Solid Films 175 (1989) 173.

[7] B.E. Yoldas, Appl. Opt. 19 (1980) 1425.

[8] A. Makishima, N. Kubo, K. Wada, Y. Kitami and T. Shimohiva, J. Am. Ceram. Soc. 69 (1986) c-127.

[9] B.E. Yoldas and D.P. Partlow, Thin Solid Films 129 (1985) 1.

[10] B.E. Yoldas, Appl. Opt. 21 (1982) 2960.

[11] R.B. Pettit and C.J. Brinker, in: Optical Coatings for Energy Efficiency and Solar Applications, SPIE 324 (1982) 176.

[12] W.L. Warren, P.M. Lenahan, C.J. Brinker, G.R. Shaffer, C.S. Ashley and S.T. Reed, in: Better Ceramics Through Chemistry IV, ed. B.J.J. Zelinski, C.J. Brinker, D.E. Clark and D.R. Ulrich, Mater. Res. Soc. Symp. Proc., Vol. 180 (Materials Research Society, Pittsburgh, PA 1990) p. 413.

[13] C.S. Ashley, S.T. Reed and A.R. Mahoney, in: Better Ceramics Through Chemistry III, ed. C.J. Brinker, D.E. Clark and D.R. Ulrich, Mater. Res. Soc. Symp. Proc., Vol. 121 (Materials Research Society, Pittsburgh, PA, 1988) p. 645.

[14] G.C. Frye, A.J. Ricco, S.J. Martin, C.J. Brinker, in: Better Ceramics Through Chemistry III, ed. C.J. Brinker, D.E. Clark and D.R. Ulrich (Materials Research Society, Pittsburgh, 1988) p. 349.

[15] T. Bein, G.C. Frye and C.J. Brinker, J. Am. Chem. Soc. 111 (1989) 7640.

[16] R.B. Pettit, C.J. Brinker and C.S. Ashley, Solar Cells 15 (1985) 267.

[17] C.J. Brinker, A.J. Hurd and K.J. Ward, in: Ultrastructure Processing of Advanced Ceramics, ed. J.D. Mackenzie and D.R. Ulrich (Wiley, New York, 1988) p. 223.

[18] A.F.M. Leenaars, K. Keizer and A.J. Burggraaf, J. Mater. Sci. 10 (1984) 1077.

[19] M.A. Anderson, M.J. Geiselmann and Q. Xu, J. Membrane Sci. 39 (1988) 243.

[20] D.P. Partlow and J. Greggi, J. Mater. Res. 2 (1987) 595.

[21] S.-I. Hirano and K. Kano, Adv. Ceram. Mater. 3 (1988) 503.

[22] S.-I. Hirano and K. Kato, J. Non-Cryst. Solids 100 (1988) 538.

[23] J. Livage and J. Lemerle, Ann. Rev. Mater. Sci. 12 (1982) 103.

[24] P. Baudy, A.C.M. Rodrigues, M.A.A. Aergerter and L.O. Bulhões, J. Non-Cryst. Solids 121 (1990) 319.

[25] S.A. Kramer, G. Kordas, J. McMillan, G.C. Hilton and D.J. Van Harlingen, Appl. Phys. Lett. 53 (1988) 156.

[26] B.D. Fabes, W.F. Doyle, B.J.J. Zelinski, L.A. Silverman and D.R. Uhlmann, J. Non-Cryst. Solids 82 (1986) 349.

[27] B.D. Fabes and G.D. Berry, J. Non-Cryst. Solids 121 (1990) 357.

[28] K.D. Budd, S.K. Dey and D.A. Payne, Br. Ceram. Proc. 36 (1985) 107.

[29] J. Fukushima, K. Kodaira and T. Matsushita, J. Mater. Sci. (1984) 595.

[30] U. Brautigam, H. Burger and W. Vogel, J. Non-Cryst. Solids 110 (1989) 663.

[31] D.I. Butts, W.C. LaCourse and S. Kim, J. Non-Cryst. Solids 110 (1988) 514.

[32] H. Schmidt, G. Rinn, R. Nass and D. Sporn, in: Better Ceramics Through Chemistry III, ed. C.J. Brinker, D.E. Clark and D.R. Ulrich, Mater. Res. Soc. Symp. Proc., Vol. 121 (Materials Research Society, Pittsburgh, PA, 1988) p. 743.

[33] F. Orgaz and F. Capel, J. Mater. Sci. 22 (1987) 1291.

[34] S.M. Melpolder and B.K. Coltrain, in: Better Ceramics Through Chemistry III, ed. C. J. Brinker, D.E. Clark and

D.R. Ulrich, Mater. Res. Soc. Symp. Proc., Vol. 121 (Materials Research Society, Pittsburgh, PA, 1988) p. 811.

[35] I. Strawbridge and P.F. James, J. Non-Cryst. Solids 86 (1986) 381.

[36] M. Guglielmi and S. Zenezini, J. Non-Cryst. Solids 121 (1990) 303.

[37] C.J. Brinker, A.J. Hurd, G.C. Frye, K.J. Ward and C.S. Ashley, J. Non-Cryst. Solids 121 (1990) 294.

[38] L.E. Scriven, in: Better Ceramics Through Chemistry III, ed. C.J. Brinker, D.E. Clark and D.R. Ulrich, Mater. Res. Soc. Symp. Proc., Vol. 121 (Materials Research Society, Pittsburgh, 1988) p. 717.

[39] A.J. Hurd and C.J. Brinker, J. Phys. (Paris) 49 (1988) 1017.

[40] C.J. Brinker and G.W. Scherer, Sol–Gel Science (Academic Press, San Diego, 1990).

[41] L.D. Landau and B.G. Levich, Acta Physiochim. URSS 17 (1942) 42.

[42] S.D.R. Wilson, J. Eng. Math. 16 (1982) 209.

[43] A.J. Hurd and C.J. Brinker, in: Better Ceramics Through Chemistry IV, ed. B.J.J. Zelinski, C.J. Brinker, D.E. Clark and D.R. Ulrich (Mater. Res. Soc. Symp. Proc., Vol. 180, Materials Research Society, Pittsburgh, 1990) p. 575.

[44] A.J. Hurd, in: The Colloidal Chemistry of Silica, ed. H. Bergna, Advances in Chemistry Series (American Chemical Society, New York) in press.

[45] D.E. Bornside, C.W. Macosko and L.E. Scriven, J. Appl. Phys. 66 (1989) 5185.

[46] S. Sakka and K. Kamiya, J. Non-Cryst. Solids 48 (1982) 31.

[47] G.W. Scherer, these Proceedings, p. 363.

[48] S.J. Gregg and K.W.S. Sing, Adsorption, Surface Area, and Porosity (Academic Press, New York, 1982).

[49] C.G.V. Burgess and D.H. Everett, J. Coll. Interf. Sci. 33 (1970) 611.

[50] W.H. Banks and W.W. Barkas, Nature 158 (1946) 341.

[51] E.D. Cohen, E.B. Gutoff and E.J. Lightfoot, in: Proc. 1990 Int. Symp. on Mechanics of thin Film Coating, A.I.Ch.E. Spring Meeting, Orlando, FL, March 1990.

[52] R.A. Yapel and L.E. Scriven, in: Proc. 1990 Int. Symp. on Mechanics of Thin Film Coating, A.I.Ch.E. Spring Meeting, Orlando, FL, March 1990.

[53] S.G. Croll, J. Appl. Polym. Sci. 23 (1979) 847.

[54] A.J. Evans, M.D. Dory, and M.S. Hu, J. Mater. Res. 3 (1988) 1043.

[55] M.D. Thouless, Acta Metall. 36 (1988) 3131.

[56] P. Meakin, Science 252 (1991) 226.

[57] A. Atkinson and R.M. Guppy, J. Mater. Sci. 26 (1991) 3869.

[58] T.J. Garino, in: Better Ceramics Through Chemistry IV, Mater. Res. Soc. Symp. Proc., Vol. 180, ed. B.J.J. Zelinski, C.J. Brinker, D.E. Clark, and D.R. Ulrich (Materials Research Society, Pittsburgh, PA, 1990) p. 497.

[59] Y. Takahashi and Y. Wada, J. Electrochem. Soc. 137 (1990) 267.

[60] T.J. Garino, PhD thesis, MIT (1988).

[61] G.C. Frye, C.J. Brinker and C.S. Ashley, unpublished results.

[62] R. Deshpande, D.-W. Hua, D.M. Smith and C.J. Brinker, J. Non-Cryst. Solids 144 (1992) 32.

[63] C.J. Brinker, G.C. Frye, A.J. Hurd and C.S. Ashley, 'Fundamentals of sol–gel dip-coating', Thin Solid Films, in press.

[64] P.M. Glaser and C.G. Pantano, J. Non-Cryst. Solids 63 (1984) 209.

[65] C.J. Brinker, A.J. Hurd, G.C. Frye, P.R. Schunk and C.S. Ashley, J. Ceram. Soc. Jpn. 99 (1991) 862.

[66] V.R. Kaufman and D. Avnir, Langmuir 2 (1986) 717.

[67] Jeffrey I. Zink and Bruce S. Dunn, J. Ceram. Soc. Jpn. 99 (1991) 878.

[68] J. Livage, M. Henry and C. Sanchez, Progr. Solid State Chem. 18 (1988) 259.

[69] T.J. Garino, private communication.